Retinal isomerization and water-pore formation in channelrhodopsin-2

Albert Ardevol[a,1] and Gerhard Hummer[a,b,1]

[a]Department of Theoretical Biophysics, Max Planck Institute of Biophysics, 60438 Frankfurt am Main, Germany; and [b]Department of Physics, Goethe University Frankfurt, 60438 Frankfurt am Main, Germany

Edited by Pablo G. Debenedetti, Princeton University, Princeton, NJ, and approved February 21, 2018 (received for review October 15, 2017)

Channelrhodopsin-2 (ChR2) is a light-sensitive ion channel widely used in optogenetics. Photoactivation triggers a *trans*-to-*cis* isomerization of a covalently bound retinal. Ensuing conformational changes open a cation-selective channel. We explore the structural dynamics in the early photocycle leading to channel opening by classical (MM) and quantum mechanical (QM) molecular simulations. With QM/MM simulations, we generated a protein-adapted force field for the retinal chromophore, which we validated against absorption spectra. In a 4-μs MM simulation of a dark-adapted ChR2 dimer, water entered the vestibules of the closed channel. Retinal all-*trans* to 13-*cis* isomerization, simulated with metadynamics, triggered a major restructuring of the charge cluster forming the channel gate. On a microsecond time scale, water penetrated the gate to form a membrane-spanning preopen pore between helices H1, H2, H3, and H7. This influx of water into an ion-impermeable preopen pore is consistent with time-resolved infrared spectroscopy and electrophysiology experiments. In the retinal 13-*cis* state, D253 emerged as the proton acceptor of the Schiff base. Upon proton transfer from the Schiff base to D253, modeled by QM/MM simulations, we obtained an early-M/P_2^{390}–like intermediate. Rapid rotation of the unprotonated Schiff base toward the cytosolic side effectively prevents its reprotonation from the extracellular side. From MM and QM simulations, we gained detailed insight into the mechanism of ChR2 photoactivation and early events in pore formation. By rearranging the network of charges and hydrogen bonds forming the gate, water emerges as a key player in light-driven ChR2 channel opening.

channelrhodopsin-2 | ChR2 | QM/MM protein modeling | optogenetics | molecular dynamics

Channelrhodopsins (ChRs) are type I rhodopsin proteins that have revolutionized neurobiology. They were first isolated in the green alga *Chlamydomonas reinhardtii* (1, 2), where they function as sensory photoreceptors for phototaxis. Their seven transmembrane helix domain anchors a retinal molecule. The retinal is covalently attached to the protein via a Schiff base linkage. Their function as light-activated ion channels makes ChRs unique in the rhodopsin family. Light absorption triggers a *trans*-to-*cis* isomerization of the C13–C14 double bond of the retinal chromophore. The strained 13-*cis* retinal moiety then induces conformational changes in the protein that open a channel through which ions can pass (3). Here we use molecular simulations and modeling with quantum mechanical (QM) and classical (molecular mechanics, MM) representations to study the early events in the photocycle of channelrhodopsin-2 (ChR2). Our aim is to gain structural and dynamic insight into the mechanism of light-driven channel opening, which provides the basis for targeted engineering of ChR2.

ChR2 has found wide application thanks to its good expression in the neurons of many organisms. Neurons expressing ChR2 can be depolarized rapidly and reversibly by illumination (4). In "optogenetics," ChR2 and other light-sensitive channels are used to control the activation/inactivation of neurons in specific locations of the brain with light. Beyond the study of neuronal circuits, ChRs are also explored as treatments of neurological disorders such as Parkinson disease, for the restoration of light sensitivity and visual capabilities, and for a wide range of biotechnological applications. Consequently, protein engineering has been used to develop ChR2 variants with desirable properties (5).

The earliest engineered ChRs were based on homology modeling (6) as well as mechanistic and structural knowledge from spectroscopic (7–9) and EM (10) data, but a major breakthrough came with the crystal structure of the C1C2 chimera in the closed (dark) state (11). The C1C2 chimera is composed of transmembrane helices H1 to H5 from ChR1, and H6 and H7 from ChR2, and exhibits activity similar to ChR2. An up to 8-Å-wide vestibule on the extracellular side of the closed-state structure (11) has been proposed to be filled with water. The vestibule points to an ion channel within the monomer, between helices H1, H2, H3, and H7. In the absence of a high-resolution open-state structure, this channel location is supported by indirect evidence. In particular, mutations of the residues along these helices can change the ion specificity of the protein (12–14). FTIR experiments probing the hydration of the helix backbone indicated that the pore length increased by only 12 Å to 16 Å upon channel opening, which requires half-formed channels already in the closed state (15).

In the structure of C1C2, the channel is blocked at the central gate by residues E90, N258, K257, E123, and D253. At this critical site, K257 forms the Schiff base with the retinal and an H bond with E123. D253 is the proton acceptor (8), and it is known that replacement of E90 by an arginine changes the ion specificity of the channel from cation- to anion-selective (13). In addition, an inner gate on the cytoplasmic side has been proposed, formed by residues Y70, E82, E83, H134, and R268 (6, 11).

Given the high sequence similarity between the C1C2 chimera and ChR2, structural and spectroscopic differences between

Significance

Channelrhodopsin-2 (ChR2) is a light-activated membrane ion channel that is widely used in biotechnological applications and optogenetics. Nonetheless, key elements of its structure, photocycle, and mechanism of action remain unresolved. We applied computational modeling and over 14 μs of molecular dynamics simulation to explore the molecular mechanism of photoactivated channel opening. Water emerges as a central player that lubricates the motions of gate residues and opens a water permeable preopen pore. By resolving the early functional dynamics of ChR2, our work also provides a foundation for the design of new variants for optogenetics applications.

Author contributions: A.A. and G.H. designed research; A.A. performed research; A.A. and G.H. analyzed data; and A.A. and G.H. wrote the paper.

The authors declare no conflict of interest.

This article is a PNAS Direct Submission.

[1]To whom correspondence may be addressed. Email: albert.ardevol@biophys.mpg.de or gerhard.hummer@biophys.mpg.de.

This article contains supporting information online at www.pnas.org/lookup/suppl/doi:10.1073/pnas.1700091115/-/DCSupplemental.

Published online March 19, 2018.

them are rather small or nonexistent (16–18). Therefore, the crystal structure of the dark-adapted C1C2 is a good approximation of the closed ChR2, and a starting point for models of the open channel. In molecular dynamics (MD) simulations, early deprotonation of E90 (in the P_1^{500}/K state) triggered a water influx from the extracellular side to form a preopen channel (19). However, the timing of E90 deprotonation remains controversial (8). Based also on MD simulations, movements of helices H2, H6, and H7 were proposed to open the cytosolic gate of C1C2 (20). These models are supported by FTIR (19), EPR (9, 21), and EM (22) experiments, but they cannot explain the role of D156 and D253 as proton donor and acceptor (8). Controversy remains about the structure, the conformational changes, and the protonation states of the central gate residue E90 during the photocycle (8, 19, 23). Recent time-resolved FTIR experiments probing the amide-I band found a temporal correlation between the conductance and the hydration of the helices (15, 23). Lórenz-Fonfría and coworkers (23) concluded that the channel is formed in two hydration steps with time constants of about 9 and 180 μs, respectively, first generating a preopen state in which the channel is filled with water, and then opening farther to create an ion-conducting state.

The photocycle of ChR2 is defined by five photochemically different species (3, 12) (Fig. 1). In the dark-adapted state, the chromophore adopts an all-*trans*-15-*anti* (24) conformation, and the channel is closed. Approximately 3 ps (7) after photon absorption, isomerization of the C13–C14 double bond results in a hot (K-like) intermediate that relaxes to the P_1^{500} state within several nanoseconds. Then, with a time constant of *ca*. 10 μs, deprotonation of the Schiff base by D253 leads to the M-like preopen channel state P_2^{390}. A concomitant water influx partially hydrates the helices. With a time constant of 180 μs, further water penetration leads to complete opening of the channel. The ion-permeable late P_2^{390} state emerges with a characteristic time of $\tau_{1/2} = 225$ μs (3, 23, 25). This transition is followed by reprotonation of the Schiff base by D156 and formation of the P_3^{520} conducting state with a time constant of 2 ms (26). The channel closes within 10 ms, but P_3^{520} can decay to either the closed D^{470} state or to a P_4^{480} inactive state that desensitizes the protein for 20 s.

Here, starting from the X-ray structure of the C1C2 chimera (11), we used MD simulations to build atomistic structural models of the D^{470} state, the K-like P_1^{500} state, and the M-like preopen P_2^{390} states (Fig. 2). For validation, we calculated UV–visible spectra that report on the conformation of the chromophore and its surrounding environment during the photocycle (27–29). To probe multimicrosecond dynamics by MD, and to relate calculated absorption spectra to experiment, we developed a protein-adapted force field for the retinal by QM/MM force matching. To model the all-*trans* to 13-*cis* isomerization of the retinal, we used metadynamics

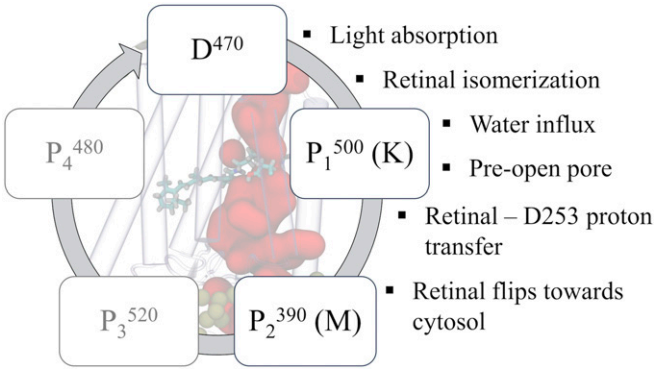

Fig. 1. Schematic representation of the intermediate states of the ChR2 photocycle and the respective protein conformational and hydration changes studied in the MD simulations.

simulations (30). The ensuing structural changes clarify why D253 is the proton acceptor; why the proton transfer is quasi-irreversible; and how the coupled dynamics of the retinal Schiff base (RSB), a bordering charge cluster, and water result in the formation of a water-conducting yet ion-impermeable preopen pore, en route to full channel activation.

Results and Discussion

RSB Reparametrization. Retinal photoactivation is a QM process. However, modeling multimicrosecond channel opening requires a computationally efficient classical description. To describe the protein-embedded and covalently bound retinal, we first developed force field parameters for the chromophore following the QM/MM force-matching approach of Doemer et al. (28). The force field parameters and charges of the chromophore were modified so that the forces in an identical classical simulation would match those of a 96-ps QM/MM MD reference simulation. The force constants of the new set of parameters (available at https://gitlab.mpcdf.mpg.de/MPIBP-Hummer/ChR-2) are somewhat softer compared with the original general amber force field (GAFF). Importantly, the relaxed bond lengths in the QM/MM simulations of the protein-bound retinal show a significant bond length alternation (BLA) between single and double bonds, $\mathrm{BLA} = \sum d_{C-C} - \sum d_{C=C}$. The QM/MM force-matching force field reproduces the QM/MM simulation ($\mathrm{BLA}_{\mathrm{QM/MM\text{-}ff}} = 0.3$), which is smaller than the one in the crystal structure ($\mathrm{BLA}_{\mathrm{X\text{-}Ray}} = 0.67$, with some uncertainty at 2.3-Å crystallographic resolution) but in agreement with previous density functional theory (DFT) simulations (28, 31) and larger than the GAFF parameters ($\mathrm{BLA}_{\mathrm{GAFF}} = 0$). As atomic partial charges, we used dynamically generated restrained electrostatic potential (D-RESP) charges averaged over the QM/MM trajectory (32) (*SI Appendix* and *SI Appendix*, Fig. S1). Compared with the standard GAFF HF/6-31G* charges, we observed a slightly higher polarization in the C13–C15 bond and around C5–C6, similar to what was reported for retinal in rhodopsin (28). Overall, the changes in bond lengths and charges are indicative of a less efficient π conjugation compared with gas phase, consistent with a blue shift in the absorption spectra of the retinal in the protein environment.

To validate the model, we calculated optical absorption spectra of the RSB, as a highly sensitive reporter on the conformation of the chromophore and its interactions with the protein. Previous studies have identified the pitfalls of not considering the thermal sampling and the protein environment when calculating the absorption spectra in rhodopsin (33). Zerner's intermediate neglect of differential overlap for spectroscopy (ZINDO/S) and time-dependent DFT computations showed the best agreement with experimental data (34). Therefore, we applied the semiempirical ZINDO/S method to a large ensemble of structures extracted from the classical and the QM/MM simulations, including all residues within 4 Å of the chromophore (*SI Appendix*). The absorption spectra calculated using snapshots from the QM/MM match perfectly with the new force field (*SI Appendix*, Fig. S2), indicating that the new parameters reproduce the QM/MM ensemble. By contrast, the GAFF simulations show significantly lower excitation energies, due to a poor description of the BLA and the chromophore–protein interactions. We attribute the discrepancy between the absolute values of the experimental and the QM/MM absorption maximum (470 and 512 nm, respectively) to the limitations of the DFT method in reproducing quantitatively the experimental BLA, which results in a red shift in the absorption spectrum (33, 35–37), and to uncertainties in the ZINDO/S method as denoted previously (28). We thus concentrate on the spectral shifts relative to the dark-adapted state, which are in excellent agreement with experiment in the M state (38), and within 10 nm in the K state (Fig. 3).

Closed-State Structure and Dynamics. Our model of the closed state is based on the C1C2 crystal structure (11) as explained in *Materials and Methods*. During the 4-μs production run, the structure remained

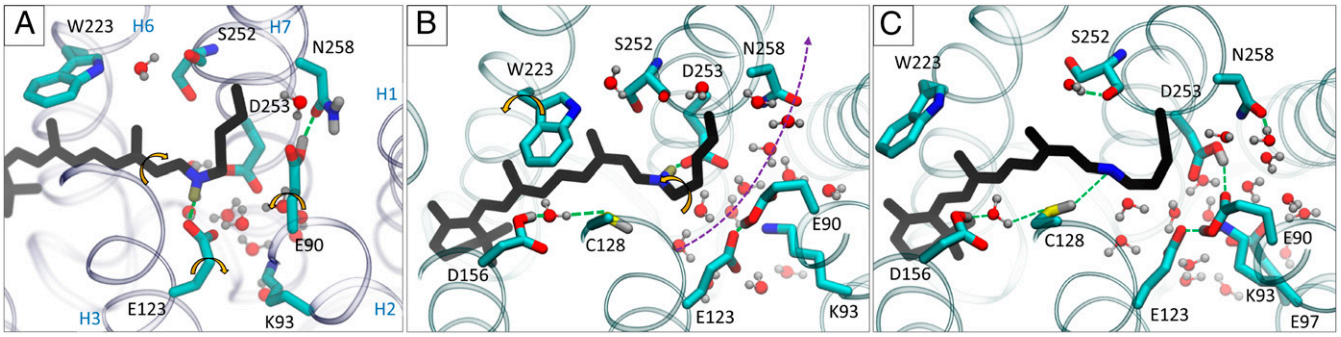

Fig. 2. Photocycle intermediates. (*A*) The D^{470} state displays the RSB H-bonding with E123. (*B*) All-*trans* to 13-*cis* isomerization of the retinal yields the K state (P_1^{500}). The RSB is pointing toward D253. E90 and E123 interact via an H bond, and a water pore is formed (indicated by a purple dashed arrow). (*C*) The M state (P_2^{390}) forms upon proton transfer from the RSB to D253. The retinal is in a planar conformation, with the nitrogen atom pointing toward the cytosolic side of the membrane. E90 is H-bonding with E123 and D253, in a hydrated central gate. W223 is displaced from its position in the dark state due to steric interactions with the C20 methyl group. The protein backbone is shown in ribbons. The yellow arrows indicate the side-chain conformational changes. H-bonding interactions are shown as dashed green lines.

stable, with a root-mean-square deviation of the transmembrane helices reaching a plateau value of ∼1.1 Å (*SI Appendix*, Fig. S3). Water molecules readily entered both sides of the channel between helices H1, H2, H3, and H7 (Fig. 4*A*), and, after about 20 ns, the number of water molecules reached the equilibrium value of 60 ± 6 molecules (*SI Appendix*, Fig. S4). Similar results were reported for previous models of ChR2 (6, 31, 39), and in simulations of related opsins (16).

We also observed structural water molecules far from the channel (*SI Appendix*, Fig. S5). In the so-called DC gate (40), a water molecule entered spontaneously from solution to bridge an H-bond interaction between residues D156 and C128. This water molecule has been observed in previous MD simulations (31, 39). Similarly, a structural water molecule mediates an H bond between the side chain of W223 and the backbone oxygen of S256. This water molecule is also present in the crystal structure of the C1C2 chimera (11) and emulates the water molecule bridging the side-chain nitrogen atom of W182 and the backbone oxygen of A215 in bacteriorhodopsin (bR) (41). Interestingly, four structural water molecules entered into the ChR2 dimer interface to bridge between helices H5, H2′, H4, and H3′, exchanging repeatedly with bulk.

A wide gap in the water density indicates the gate of the putative ion channel. Residues K257 (and the RSB), N258, E90, E123, and D253 form the bottleneck that blocks the leakage of water, protons, and ions (Figs. 2*A* and 4*A*). A dense network of interhelical interactions of helix H7 with helices H2 and H3 preclude further penetration of water molecules and ions. E123 (H3) forms a stable salt bridge with the protonated nitrogen, in agreement with the crystal structure of C1C2 (11) and with previous MD simulations of ChR2 (19) and C1C2 (16). Previous QM/MM MD simulations of ChR2 showed alternative RSB–water and RSB–D253 interactions (31). In our simulation, the closed-state structure gives no indication that later, in the P_1^{500}/K state, D253 becomes the proton acceptor. This conundrum will be addressed in the following section.

While the paper was under revision, the crystal structures of the dark (closed) state of the wild type and the C128T mutant of ChR2 were published (42). As described in *SI Appendix* and shown in *SI Appendix*, Fig. S13, our model accurately captures protein, cofactor, and hydration structures.

Formation of the Preopen Pore. The photocycle of ChR2 begins with light absorption and isomerization of the C13–C14 double bond of the RSB moiety. This local conformational change triggers a cascade of events that leads to the preopen channel, the conducting state, desensitized structures, and, ultimately, back to the dark-adapted state (Fig. 1). Previous models of the 13-*cis* RSB photointermediate have been constructed by structural superposition of the D^{470} (dark) state with the crystal structure of the K state of bR (43) followed by geometry optimization of the 13-*cis* RSB coordinates in ChR2 (20); by a stepwise tilting of the C13–C14 torsion and MD equilibration steps—all of the RSB torsions were fixed during the equilibration MDs in a sort of big-steps umbrella sampling simulation (19); or by modeling the RSB in the all-*trans* configuration (44). Here we adopted a more flexible strategy based on enhanced sampling simulations. Starting from various initial structures from our equilibrium trajectory of the D^{470} state, we ran a series of metadynamics simulations (30) as described in *SI Appendix*. The metadynamics simulations were performed using the ground-state force field parameters for the retinal. This simplification does not include the effect of photoexcitation on the electronic structure of the retinal and on the isomerization energy barrier. We used the C13–C14 torsion as reaction coordinate, and restrained the neighboring torsions with a smoothed-wall potential to avoid the double-torsion flip that leads to the 13-*cis*–15-*syn* conformation. This isomer has also been observed in the D^{470} state (45) and corresponds to a closed (nonconducting) channel state.

Computational isomerization of the chromophore led to a P_1^{500} state with a strained (hot) 13-*cis*–15-*anti* conformation (Fig. 2*B*). During the isomerization, the nitrogen of the Schiff base changed its orientation by ∼90°, away from its dark-state partner E123 to form an H bond with D253. A twist of the retinal ethylene chain (C13 to C15) and the C20 methyl group pushes the side chain of F226 toward H6. Interestingly, the change in the orientation of the nitrogen atom of the RSB toward D253 resembles the conformational change of the RSB in the K and L states of bR, as observed by X-ray crystallography (43, 46–48). Two of these structures (43, 47) also show that the C20 methyl tilts toward Y185 (equivalent to F226 in ChR2), and Matsui et al. (43) reported the tilting of the side chain of Y185 as a response to the >1-Å displacement of the C20 methyl group. By contrast, the earliest structure of the K state in bR (49) does not show any of these changes. Overall, the pathway of retinal isomerization in ChR2 resembles that in bR (7).

As another similarity of bR and ChR2, tilting of the Schiff base remodels the H-bond networks in the gate region. In bR, the Schiff base is H-bonding with a water molecule in the dark state, but this water is disordered in the K state (47, 49), or moved (43, 46). The water displacement facilitates the first proton transfer event (48, 49) and provokes a movement of the Schiff base toward the cytoplasmic side of the channel. In the dark state of ChR2, the RSB is H-bonding with E123. Isomerization of the C13–C14 bond and H-bond partner change of the

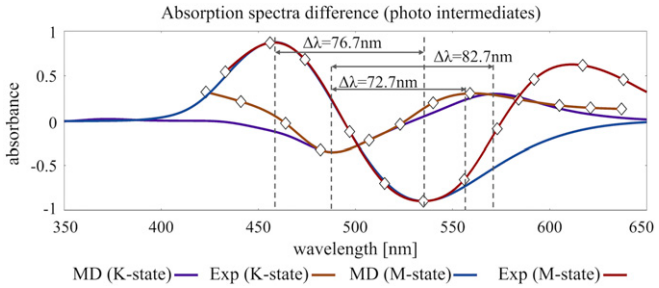

Fig. 3. Differential absorbance changes of ChR2 K- and M-state photointermediates from simulation (purple and blue lines, respectively) and experiment (orange and red lines, respectively) (10). The experimental curves are shifted by 42 and 75 nm, and the intensities are scaled by 0.7 and 1.05 and shifted by 0.12 and 0.15 units for the K and M states, respectively.

RSB leave E123 free. This transition is accompanied by an influx of water molecules, which facilitates the cleavage of E90–N258 and formation of E90–E123 H-bond interactions. This implies that, as a result of the photoisomerization, H2–H7 and H3–H7 interhelical interactions are replaced by H2–H3 and H7–H7 (RSB–D253) interactions. This is in agreement with FTIR data showing changes in the H-bonding pattern and strength already in the K-like intermediate (50). The differential absorption spectra of the P_1^{500} photointermediate shows good agreement with experiment (Fig. 3), supporting our model.

Water Dynamics. As a consequence of H-bond remodeling, a preopen pore forms, as indicated by a continuous band of water density between the two vestibules (Fig. 4*B*). We defined a cylindrical volume centered between helices H1, H2, H3, and H7 that covers the pore between opposite sides of the lipid membrane (*SI Appendix*, Fig. S6). Then we monitored the evolution of the water density in the z (transmembrane) direction in time. In the dark state, the water density is zero at the center of the channel (i.e., in the central gate), leaving a gap or bottleneck of unsolvated protein residues. The length of the gap was defined as the maximum extent in the *z* direction of regions below a minimum threshold of water density. *SI Appendix*, Fig. S7 shows the evolution of the gap length in time for the states modeled. The closed or dark-adapted state (D^{470}) displays a large gap that is persistent during the whole trajectory. By contrast, the first photoactivated state shows that, ∼0.6 μs after isomerization, the gap vanishes and stays closed for the rest of the simulation. The active site after the isomerization is more hydrated compared with the dark state. The influx of water molecules modifies some of the H1–H2, H2–H7, and H3–H7 interhelical interactions, inducing conformational changes in the side-chain orientation of several residues of the pore. Cleavage of these interactions, which form a tight mesh of contacts in the dark state that keep the channel closed, let water molecules flow across the pore after retinal isomerization.

We characterized the water permeation by calculating the potential of mean force (PMF) and the position-dependent diffusion coefficient along the transmembrane direction in the pore. We accomplished this by using a maximum likelihood approach based on the transition matrix (51). *SI Appendix*, Fig. S8 shows the PMF and the diffusion coefficient evolution in time (using time windows of 250 ns of MD simulation). The PMF shows a high barrier at the central gate for the first time window (0 μs to 0.25 μs) that prevents water flux. However, this barrier disappears ∼0.5 μs after isomerization. The diffusion coefficient shows a nearly flat profile, indicating that the calculated PMF is reliable and that there is no other major variable needed to describe the water flux.

Even though water can pass through the gate, we did not observe a spontaneous ion permeation event in any of our simulations. To rule out that this is an artifact of the simulation conditions, we performed a series of MD simulations with increased ion concentration and with the effect of an external electric field. The absence of ion permeation in any of these simulations agrees with the experimental observation of water influx into ChR2 early in the photocycle (<10 μs) into a nonconducting state (15). According to the experiments, the conducting channel is only observed at later stages of the P_2^{390} intermediate and upon formation of P_3^{520}. Based on the area of the amide-I band, approximately a third of the total of 10 water molecules present in the conducting state enter the channel in the preopen state (15). To compare directly to the experiments, we calculated the number of water molecules that are in H-bonding interaction with the backbone carbonyls of the helices. We observed an increase by 3.2 and 4.4 water molecules in the K- and the M-state MD simulations, respectively (*SI Appendix*, Fig. S9 and Table S1). As anticipated, only helices H1, H2, H3, and H7 showed a change in hydration. We conclude that the simulation captures the first helix solvation event observed experimentally (15).

Structure of the M-Like P_2^{390} Intermediate. The transition from the P_1^{500} to the P_2^{390} state reflects the proton transfer from the RSB to D253. Indeed, QM/MM MD simulations (including the RSB and the proton acceptor in the quantum region; see *SI Appendix*) showed that the proton can jump spontaneously to D253. This proton transfer process is remarkably different in bR. In bR, the proton acceptor is $D85/E123_{ChR2}$. Proton transfer in bR is mediated by a bridging water molecule and/or $T89_{bR}$ (47, 52, 53), which establish a hydrogen bond network from the RSB to $D85_{bR}$. After proton transfer, the ionic form of $D212_{bR}$ is stabilized by H-bonding interactions to $Y185_{bR}$, while $D85_{bR}$ is protonated. In ChR2, the proton transfer takes place in the K state, where the RSB is pointing toward $D253_{ChR2}$ and does not require any bridging residue or water molecule. After proton transfer, flipping of the RSB toward the cytosolic side makes the process quasi-irreversible. The protein environment is also different, favoring the neutral form of D253 (which cannot H-bond to $F226/Y185_{bR}$) and stabilizing the ionic form of $E123/D85_{bR}$ by H-bonding interactions with E90 and K93. Therefore, the mechanism and the thermodynamics in ChR2 are substantially different from that of bR.

We simulated the P_2^{390} M intermediate in ChR2 by manually transferring the proton from the RSB to D253 in seven structures taken from our K-like ensemble and extending classical MD simulations for 1 μs each. In six out of seven trajectories, after 200 ns to 400 ns of MD simulation, the unprotonated retinal underwent a conformational change that oriented the nitrogen atom toward the cytosolic side (Fig. 2*C*). As expected after proton transfer, the absorption spectrum of this conformation

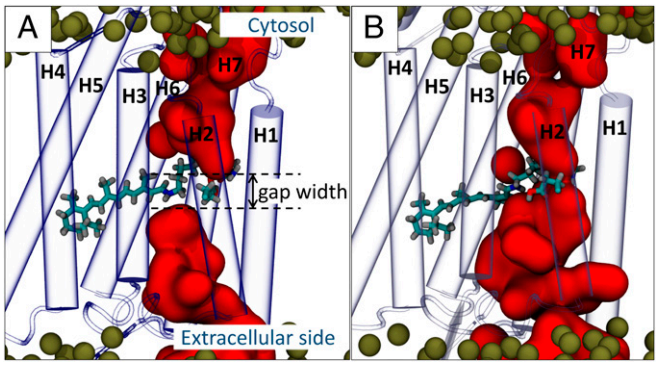

Fig. 4. Water density (in red) of (*A*) a snapshot of the D^{470} structure, which presents a gap in the center of the channel near the retinal, K257, N258, and E90 (shown in licorice), and (*B*) a snapshot of the water pore after photoisomerization of the retinal. The head groups of the lipids are shown as tan spheres, and one of the chains of ChR2 is shown as transparent blue cartoon. The rest of the system is omitted for clarity.

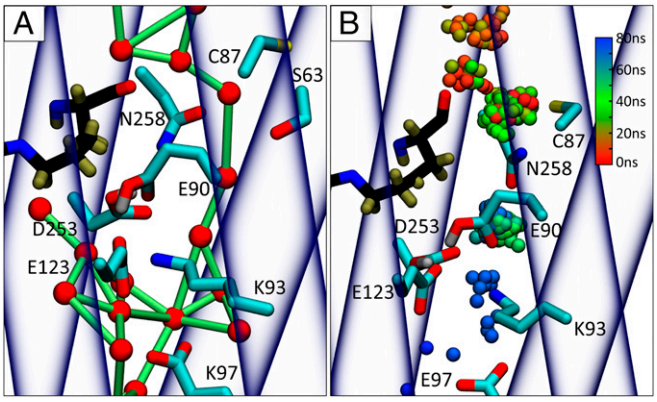

Fig. 5. Water preopen pore in the M state. (*A*) Connectivity of the water molecules. Lime bonds connect water molecules (red) within 4-Å distance. (*B*) Trajectory of a water permeation event. The oxygen atom of the water molecule is represented as a sphere colored according to the permeation time (as indicated by the color bar).

shows a large blue shift compared with the dark-adapted state. The difference spectra between the dark and the M states are in perfect agreement with experiment, as shown in Fig. 3. QM/MM MD simulations of the M state show a nearly identical geometry with a more accurate absorption spectrum due to a better description of the BLA (*SI Appendix*, Fig. S10). The change in the orientation of the Schiff base makes the proton transfer reaction quasi-irreversible, positioning it for eventual reprotonation. In this conformation, the retinal moiety adopts a nearly planar structure, and steric interactions of the C20 methyl group induce a displacement of W223 toward the cytosolic side. This effect was also observed in the X-ray structures of the M state in bR, where the C20 methyl group pushes on $W182_{bR}/W223_{ChR2}$ (47, 48, 54), and in a theoretical study of the C1C2 chimera (20). In ChR2, this displaces the structural water bound to W223. These motions have been suggested as a mechanism by which the photoisomerization of the retinal induces large conformational changes at the cytoplasmic side of helix H6 (55).

The orientation of the RSB toward the cytosol shortens the distance between the Schiff base and the eventual proton donor D156 from ∼10.5 Å in the D^{470} state to ∼9 Å in the M-like state. This distance is still too large for a direct proton transfer, but it could be bridged by a water molecule and C128, as the distance between the Schiff base and the cysteine is also reduced (*SI Appendix*, Fig. S11). D253 shares H-bond interactions with E90, E123, K93, N258, and the newly entered water molecules in the active site (*SI Appendix*, Fig. S12).

In the M-like state the water pore remains open. Water molecules diffuse through the channel in a series of jumps between local water sites. Fig. 5 shows the water connectivity in the channel and the path of a water molecule crossing the central gate between E90 and N258 from the cytosolic to the extracellular sides of the membrane. In P_2^{390}, helix 2 preserves the tilting angle and intercysteine distances of the dark state (*SI Appendix*, Table S2). The distance changes seen in EPR experiments (9, 21) and the tilting angle change in MD simulations (19) should thus take place later in the photocycle, i.e., in the P_3^{500} state and/or after deprotonation of the E90 residue. The structure of the extracellular side of the central gate shows a complex H-bond network between residues D253 (protonated), E90 (protonated), E123, K93, E97, R120, and H249, providing a suitable route for proton transfer to the extracellular side.

Conclusions

Water emerges as a major factor in ChR2 conformational dynamics and channel activation. Light-induced rearrangements in a charge cluster bordering the RSB trigger the influx of water and the formation of a water-conducting but ion-impermeable preopen pore. As a result of 13-*cis* photoisomerization, the retinal also exchanges its H-bonding partner from E123 to D253. We found, in QM/MM simulations, that the Schiff base and D253 share a proton, with frequent back-and-forth proton transfer reactions. After proton transfer, the retinal flips, D253 swings away, and an M-like structure is formed, in which the Schiff base points toward the cytosol. This trapdoor-like rearrangement makes the overall proton translocation directional, in effect preventing reprotonation from the extracellular side. Simulations thus allowed us to address two major open questions: the initial steps of light-driven pore opening, and the unidirectionality of the proton transfer reactions and, in turn, of the photocycle.

A critical element of the simulations was an accurate chromophore model. QM/MM force-matching force field parameters of the retinal chromophore in ChR2 allowed us to simulate ChR2 in various states for >14 μs, matching the experimental structure and capturing measured absorption spectra.

With this model, studies of full channel opening on even longer time scales come within reach. Following the prepore opening seen in the simulations, experiments indicate a further widening of the channel in ChR2 by a second influx of water molecules at *ca*. 200 μs (15). For bR, it has been speculated that water influx is driven, in part, by unbalanced charges and strong local electric fields (56). It is conceivable that similar effects contribute to a water-driven pore widening and channel formation also in ChR2, as deprotonation of D156 and reprotonation of the Schiff base are crucial for formation of the P_3^{500} state, in which ion conductance is maximal. The work presented provides computational tools and atomistic structural and mechanistic information about the ChR2 photocycle that can serve as the basis for the modeling of further photointermediates and for ChR2 engineering.

Materials and Methods

ChR2 Modeling. The structure of the closed state of *C. reinhardtii* ChR2 was constructed by homology modeling based on the crystal structure of the C1C2 chimera—PDB ID 3UG9 (11)—and the Swiss-Model software (57). The protonation states of all residues were chosen based on the physiological pH and their local environment. Based on FTIR experimental data (8), E90 and D156 were modeled in their nonionic form. All crystallographic waters were kept, and the system was embedded in a 1-palmitoyl-2-oleoyl-*sn*-glycero-3-phosphocholine (POPC) lipid bilayer. A ChR2 dimer was solvated with TIP3P water molecules (58) and 100 mM NaCl and enclosed in an $81 \times 80 \times 166$ $Å^3$ box. The protein was modeled using the AMBER99-SB (59, 60) all-atom force field with side-chain torsional angle corrections (61), and the lipids were modeled with the GAFFlipid force field (62). The chromophore was modeled with an ad hoc set of QM/MM force-matching parameters (28) (*SI Appendix*). All classical MD simulations were run with the NAMD 2.9 software (63). The geometry of the initial complex was optimized by a series of energy minimization cycles. Then, the system was thermalized and equilibrated to 300 K, followed by an MD simulation of the D^{470}state in the NPγT ensemble for 4 μs.

Water Permeation. The PMF and the position-dependent diffusion coefficient $D(z)$ of water permeation through the channel were calculated using a maximum likelihood method (64). First, a transition matrix was calculated by dividing the pore into 11 bins and counting all transitions for all water molecules in windows of 260 ns at different time lags. Then, the equilibrium probabilities P_i and the rate coefficients $R_{j,i}$ were optimized to maximize the likelihood of the observed transition matrix. Finally, the PMF and $D(z)$ were obtained from probabilities and rates. *SI Appendix*, Fig. S8 shows the transition matrices, the PMF, and the diffusion coefficient before and after channel opening in the simulation of the photointermediate P_1^{500}.

ACKNOWLEDGMENTS. We thank Dr. Christian Bamann for fruitful discussions. This project has received funding from the European Union's Horizon 2020 research and innovation programme under Marie Sklodowska-Curie Grant Agreement 661784. This work was supported by the Max Planck Society.

1. Nagel G, et al. (2002) Channelrhodopsin-1: a light-gated proton channel in green algae. *Science* 296:2395–2398.
2. Nagel G, et al. (2003) Channelrhodopsin-2, a directly light-gated cation-selective membrane channel. *Proc Natl Acad Sci USA* 100:13940–13945.
3. Lórenz-Fonfría VA, Heberle J (2014) Channelrhodopsin unchained: structure and mechanism of a light-gated cation channel. *Biochim Biophys Acta* 1837:626–642.
4. Nagel G, et al. (2005) Light activation of channelrhodopsin-2 in excitable cells of *Caenorhabditis elegans* triggers rapid behavioral responses. *Curr Biol* 15:2279–2284.
5. Wietek J, Prigge M (2016) *Enhancing Channelrhodopsins: An Overview. Optogenetics: Methods and Protocols, Methods in Molecular Biology*, ed Kianianmomeni A (Humana, Totowa, NJ), Vol 1408, pp 141–165.
6. Watanabe HC, Welke K, Sindhikara DJ, Hegemann P, Elstner M (2013) Towards an understanding of channelrhodopsin function: simulations lead to novel insights of the channel mechanism. *J Mol Biol* 425:1795–1814.
7. Verhoefen MK, et al. (2010) The photocycle of channelrhodopsin-2: ultrafast reaction dynamics and subsequent reaction steps. *ChemPhysChem* 11:3113–3122.
8. Lórenz-Fonfría VA, et al. (2013) Transient protonation changes in channelrhodopsin-2 and their relevance to channel gating. *Proc Natl Acad Sci USA* 110:E1273–E1281.
9. Sattig T, Rickert C, Bamberg E, Steinhoff HJ, Bamann C (2013) Light-induced movement of the transmembrane helix B in channelrhodopsin-2. *Angew Chem Int Ed Engl* 52:9705–9708.
10. Müller M, Bamann C, Bamberg E, Kühlbrandt W (2011) Projection structure of channelrhodopsin-2 at 6 Å resolution by electron crystallography. *J Mol Biol* 414: 86–95.
11. Kato HE, et al. (2012) Crystal structure of the channelrhodopsin light-gated cation channel. *Nature* 482:369–374.
12. Schneider F, Grimm C, Hegemann P (2015) Biophysics of Channelrhodopsin. *Annu Rev Biophys* 44:167–186.
13. Wietek J, et al. (2014) Conversion of channelrhodopsin into a light-gated chloride channel. *Science* 344:409–412.
14. Berndt A, Lee SY, Ramakrishnan C, Deisseroth K (2014) Structure-guided transformation of channelrhodopsin into a light-activated chloride channel. *Science* 344: 420–424.
15. Lórenz-Fonfría VA, et al. (2015) Temporal evolution of helix hydration in a light-gated ion channel correlates with ion conductance. *Proc Natl Acad Sci USA* 112: E5796–E5804.
16. VanGordon MR, Gyawali G, Rick SW, Rempe SB (2017) Atomistic study of intramolecular interactions in the closed-state channelrhodopsin chimera, C1C2. *Biophys J* 112:943–952.
17. Dokukina I, Weingart O (2015) Spectral properties and isomerisation path of retinal in C1C2 channelrhodopsin. *Phys Chem Chem Phys* 17:25142–25150.
18. Inaguma A, et al. (2015) Chimeras of channelrhodopsin-1 and -2 from *Chlamydomonas reinhardtii* exhibit distinctive light-induced structural changes from channelrhodopsin-2. *J Biol Chem* 290:11623–11634.
19. Kuhne J, et al. (2015) Early formation of the ion-conducting pore in channelrhodopsin-2. *Angew Chem Int Ed Engl* 54:4953–4957.
20. Takemoto M, et al. (2015) Molecular dynamics of channelrhodopsin at the early stages of channel opening. *PLoS One* 10:e0131094.
21. Krause N, Engelhard C, Heberle J, Schlesinger R, Bittl R (2013) Structural differences between the closed and open states of channelrhodopsin-2 as observed by EPR spectroscopy. *FEBS Lett* 587:3309–3313.
22. Müller M, Bamann C, Bamberg E, Kühlbrandt W (2015) Light-induced helix movements in channelrhodopsin-2. *J Mol Biol* 427:341–349.
23. Kottke T, Lórenz-Fonfría VA, Heberle J (2017) The grateful infrared: Sequential protein structural changes resolved by infrared difference spectroscopy. *J Phys Chem B* 121:335–350.
24. Becker-Baldus J, et al. (2015) Enlightening the photoactive site of channelrhodopsin-2 by DNP-enhanced solid-state NMR spectroscopy. *Proc Natl Acad Sci USA* 112: 9896–9901.
25. Bamann C, Kirsch T, Nagel G, Bamberg E (2008) Spectral characteristics of the photocycle of channelrhodopsin-2 and its implication for channel function. *J Mol Biol* 375: 686–694.
26. Nack M, et al. (2012) Kinetics of proton release and uptake by channelrhodopsin-2. *FEBS Lett* 586:1344–1348.
27. Stehfest K, Hegemann P (2010) Evolution of the channelrhodopsin photocycle model. *ChemPhysChem* 11:1120–1126.
28. Doemer M, Maurer P, Campomanes P, Tavernelli I, Rothlisberger U (2014) Generalized QM/MM force matching approach applied to the 11-cis protonated Schiff base chromophore of rhodopsin. *J Chem Theory Comput* 10:412–422.
29. Suomivuori CM, Gamiz-Hernandez AP, Sundholm D, Kaila VRI (2017) Energetics and dynamics of a light-driven sodium-pumping rhodopsin. *Proc Natl Acad Sci USA* 114: 7043–7048.
30. Laio A, Parrinello M (2002) Escaping free-energy minima. *Proc Natl Acad Sci USA* 99: 12562–12566.
31. Guo Y, et al. (2016) Active site structure and absorption spectrum of channelrhodopsin-2 wild-type and C128T mutant. *Chem Sci* 7:3879–3891.
32. Maurer P, Laio A, Hugosson HW, Colombo MC, Rothlisberger U (2007) Automated parametrization of biomolecular force fields from quantum mechanics/molecular mechanics (QM/MM) simulations through force matching. *J Chem Theory Comput* 3: 628–639.
33. Valsson O, Campomanes P, Tavernelli I, Rothlisberger U, Filippi C (2013) Rhodopsin absorption from first principles: Bypassing common pitfalls. *J Chem Theory Comput* 9: 2441–2454.
34. López CS, Faza ON, Estévez SL, de Lera AR (2006) Computation of vertical excitation energies of retinal and analogs: scope and limitations. *J Comput Chem* 27:116–123.
35. Coccia E, Varsano D, Guidoni L (2013) Protein field effect on the dark state of 11-*cis* retinal in rhodopsin by quantum Monte Carlo/molecular mechanics. *J Chem Theory Comput* 9:8–12.
36. Bravaya K, Bochenkova A, Granovsky A, Nemukhin A (2007) An opsin shift in rhodopsin: retinal S0-S1 excitation in protein, in solution, and in the gas phase. *J Am Chem Soc* 129:13035–13042.
37. Altun A, Yokoyama S, Morokuma K (2008) Spectral tuning in visual pigments: an ONIOM(QM:MM) study on bovine rhodopsin and its mutants. *J Phys Chem B* 112: 6814–6827.
38. Bamann C, Gueta R, Kleinlogel S, Nagel G, Bamberg E (2010) Structural guidance of the photocycle of channelrhodopsin-2 by an interhelical hydrogen bond. *Biochemistry* 49:267–278.
39. Watanabe HC, et al. (2012) Structural model of channelrhodopsin. *J Biol Chem* 287: 7456–7466.
40. Nack M, et al. (2010) The DC gate in Channelrhodopsin-2: crucial hydrogen bonding interaction between C128 and D156. *Photochem Photobiol Sci* 9:194–198.
41. Luecke H, Schobert B, Richter HT, Cartailler JP, Lanyi JK (1999) Structure of bacteriorhodopsin at 1.55 A resolution. *J Mol Biol* 291:899–911.
42. Volkov O, et al. (2017) Structural insights into ion conduction by channelrhodopsin 2. *Science* 358:eaan8862.
43. Matsui Y, et al. (2002) Specific damage induced by X-ray radiation and structural changes in the primary photoreaction of bacteriorhodopsin. *J Mol Biol* 324:469–481.
44. Richards R, Dempski RE (2017) Adjacent channelrhodopsin-2 residues within transmembranes 2 and 7 regulate cation selectivity and distribution of the two open states. *J Biol Chem* 292:7314–7326.
45. Nack M, Radu I, Bamann C, Bamberg E, Heberle J (2009) The retinal structure of channelrhodopsin-2 assessed by resonance Raman spectroscopy. *FEBS Lett* 583: 3676–3680.
46. Schobert B, Cupp-Vickery J, Hornak V, Smith S, Lanyi J (2002) Crystallographic structure of the K intermediate of bacteriorhodopsin: conservation of free energy after photoisomerization of the retinal. *J Mol Biol* 321:715–726.
47. Nango E, et al. (2016) A three-dimensional movie of structural changes in bacteriorhodopsin. *Science* 354:1552–1557.
48. Lanyi JK, Schobert B (2003) Mechanism of proton transport in bacteriorhodopsin from crystallographic structures of the K, L, M1, M2, and M2′ intermediates of the photocycle. *J Mol Biol* 328:439–450.
49. Edman K, et al. (1999) High-resolution X-ray structure of an early intermediate in the bacteriorhodopsin photocycle. *Nature* 401:822–826.
50. Radu I, et al. (2009) Conformational changes of channelrhodopsin-2. *J Am Chem Soc* 131:7313–7319.
51. Best RB, Hummer G (2010) Coordinate-dependent diffusion in protein folding. *Proc Natl Acad Sci USA* 107:1088–1093.
52. Lanyi JK (2004) Bacteriorhodopsin. *Annu Rev Physiol* 66:665–688.
53. Wolter T, Welke K, Phatak P, Bondar AN, Elstner M (2013) Excitation energies of a water-bridged twisted retinal structure in the bacteriorhodopsin proton pump: a theoretical investigation. *Phys Chem Chem Phys* 15:12582–12590.
54. Sass HJ, et al. (2000) Structural alterations for proton translocation in the M state of wild-type bacteriorhodopsin. *Nature* 406:649–653.
55. Subramaniam S, Henderson R (2000) Molecular mechanism of vectorial proton translocation by bacteriorhodopsin. *Nature* 406:653–657.
56. Hummer G (2007) Water, proton, and ion transport: From nanotubes to proteins. *Mol Phys* 105:201–207.
57. Biasini M, et al. (2014) SWISS-MODEL: modelling protein tertiary and quaternary structure using evolutionary information. *Nucleic Acids Res* 42:W252–W258.
58. Jorgensen WL, Chandrasekhar J, Madura JD, Impey RW, Klein ML (1983) Comparison of simple potential functions for simulating liquid water. *J Chem Phys* 79:926–935.
59. Cheatham TE, 3rd, Cieplak P, Kollman PA (1999) A modified version of the Cornell et al. force field with improved sugar pucker phases and helical repeat. *J Biomol Struct Dyn* 16:845–862.
60. Hornak V, et al. (2006) Comparison of multiple Amber force fields and development of improved protein backbone parameters. *Proteins* 65:712–725.
61. Lindorff-Larsen K, et al. (2010) Improved side-chain torsion potentials for the Amber ff99SB protein force field. *Proteins* 78:1950–1958.
62. Dickson CJ, Rosso L, Betz RM, Walker RC, Gould IR (2012) GAFFlipid: A general Amber force field for the accurate molecular dynamics simulation of phospholipid. *Soft Matter* 8:9617–9627.
63. Phillips JC, et al. (2005) Scalable molecular dynamics with NAMD. *J Comput Chem* 26: 1781–1802.
64. Hummer G (2005) Position-dependent diffusion coefficients and free energies from Bayesian analysis of equilibrium and replica molecular dynamics simulations. *New J Phys* 7:34.